Article

Creep-Fatigue Life Evaluation for Grade 91 Steels with Various Origins and Service Histories

Haruhisa Shigeyama [1,*], Yukio Takahashi [1], John Siefert [2] and Jonathan Parker [2]

1 Central Research Institute of Electric Power Industry, Yokosuka 240-0196, Japan; yukio@criepi.denken.or.jp
2 Electric Power Research Institute, Charlotte, NC 28262, USA; jsiefert@epri.com (J.S.); jparker@epri.com (J.P.)
* Correspondence: haruhisa@criepi.denken.or.jp; Tel.: +81-70-5589-6109

Abstract: Grade 91 steel is widely used in the boilers and piping of thermal power plants. There has been significant research interest in understanding the variations in creep characteristics among different heats of this steel for effective plant management. In recent years, thermal power plants have been subjected to frequent load changes and startup/shutdown to adjust power supply and demand and stabilize frequencies. These operational shifts have raised concerns regarding the potential for creep-fatigue damage in high-temperature components. Therefore, this research focuses on creep-fatigue properties of Grade 91 steel and their predictability. Tensile, creep, strain-controlled fatigue, and strain-controlled creep-fatigue tests were performed on six Grade 91 steels with different heats and/or histories, and the characteristics in each test were compared. As a result, the variations in creep-fatigue life among the materials were found to be correlated with the difference in creep characteristics and stress level during stress relaxation. Furthermore, the study involved a comparative assessment of the predictive performance of creep-fatigue life using five different approaches: time fraction, classical ductility exhaustion, modified ductility exhaustion, energy-based, and hybrid approaches. Among these approaches, the hybrid approach, based on inelastic strain energy density at fracture formulated as a function of inelastic strain rate, exhibited the most accurate predictive performance.

1. Introduction

Grade 91 steel is a type of creep strength-enhanced ferritic steel, and it is widely employed in piping and pressure vessels within conventional thermal power boilers across the globe. Additionally, it has also been used in heat-recovery steam generators for gas–turbine combined cycle power generation. It is important to accurately evaluate the creep life of high-temperature components to properly maintain and manage the plants. However, recent research has highlighted significant variations in the creep rupture life and creep rupture ductility among different heats of Grade 91 steel [1–12]. Kimura et al. [1,2] and Sawada et al. [5] extensively investigated long-term creep rupture specimens of Grade 91 steel from multiple heats and pointed out that the creep strength in the long-term region at 600 °C is related to the Ni content. They indicated that higher Ni content leads to a reduction in MX fine precipitates and the coarsening of Z phase in the long-term region, resulting in decreased creep strength. Additionally, in heats containing the δ-ferrite phase, they noted a consistent trend of lower creep strength from the short-term to long-term regions compared to other heats [2]. Furthermore, Sawada et al. [11] pointed out the influence of chromium layer segregation on the heat dependence of creep strength in Grade T91 tube materials from multiple heats. Maruyama et al. [6,12] analyzed creep rupture data from Grade 91 steel with multiple heats and pointed out that the causes of heat dependence vary depending on the creep test conditions. They claimed that creep

strength at low temperatures and high stresses correlates with post-tempering hardness, while creep strength at high temperatures and intermediate rupture times is influenced by both hardness and Cr concentration. They also asserted that creep strength in long-term rupture is correlated with the size of the prior austenite grain. The Electric Power Research Institute (EPRI) conducted a detailed analysis of several heats of Grade 91 steel taken from an ex-serviced header with approximately 79,000 h of operation [3,4]. Based on their findings, they proposed new chemical composition specifications to improve the material's creep strength and ductility [4]. This recommendation was incorporated into the American Society for Mechanical Engineers (ASME) Boiler and Pressure Vessel Code (BPVC) as Code Case 2864 [13], designating it as Grade 91 Type 2.

In recent years, variable power sources such as solar and wind power generation have been introduced in large numbers in many countries to achieve carbon neutrality. Therefore, thermal power plants have been subject to frequent load changes and startups/stops to adjust power supply–demand and stabilize frequencies. This trend will become even stronger in the future. This change in operating mode increases the risk of creep-fatigue failure in high-temperature components. However, there has not been sufficient discussion about the variations in creep-fatigue life among different Grade 91 steels.

Many methods have been proposed to date for evaluating creep-fatigue damage in high-temperature components. The ASME BPVC Section III Division 5 [14], one of the typical design codes for addressing creep-fatigue loading, employs a time fraction approach to evaluate creep damage during strain holding. The R5 [15], which provides assessment procedures for creep-fatigue life, uses a ductility exhaustion approach to calculate creep damage. These methods encompass the fundamental concepts of creep-fatigue life evaluation, with the former being understood as a stress-based approach and the latter as an inelastic strain-based one. Various variations of the ductility exhaustion approach have been proposed, including a modified ductility exhaustion approach [16] proposed by one author. A comprehensive review of creep ductility, a pivotal aspect in the ductility exhaustion approach, is presented in [17]. Additionally, several evaluation methods have been proposed that are not based on simple stress or inelastic strain but on inelastic strain energy [18–21]. These energy-based approaches employ inelastic strain energy density instead of inelastic strain in the ductility exhaustion approach as a driving force of creep damage. In recent years, these strain energy-based evaluation methods have been further developed to account for average stress [22,23] and damage due to oxidation [23,24]. Additionally, improvements have been made to apply them to complex loading conditions, such as a combination of large and small strain variations [25] and a combination of strain-controlled and stress-controlled loading [26,27]. Furthermore, a hybrid approach has been also suggested, which considers the critical inelastic strain energy density to be dominated by the inelastic strain rate [28,29].

This research focuses on the variation in creep-fatigue life among materials and its predictability. A series of tests, including tensile, creep, strain-controlled fatigue, and strain-controlled creep-fatigue tests, was carried out on six Grade 91 steels with different heats and/or histories. Consequently, the material-dependent characteristics in each test were clarified. In addition, the creep-fatigue lives of these materials under various test conditions were predicted using five approaches: the time fraction, the classical ductility exhaustion, the modified ductility exhaustion, the energy-based, and the hybrid approaches. Then, the predictive performance of each approach was compared.

2. Materials and Methods

2.1. Materials

Six Grade 91 steels, designated as A to F, were investigated in this study. Materials A and B were new materials without any usage history in power plants. Material A was procured in plate form with dimensions of $1000 \times 1000 \times 50$ mm, while Material B was obtained in pipe form with dimensions of 318.5 mm in outer diameter and 32 mm in thickness. Material A underwent normalization at 1060 °C for 90 min, followed by

tempering at 760 °C for 60 min. Material B underwent normalization at 1060 °C for 10 min, followed by tempering at 780 °C for 46 min. Materials C, D, E, and F were sourced from two ex-service headers. Materials C and F came from the same header, which had been in service for about 79,000 h. Material C was taken from P91 barrel section, whereas material F was taken from an F91-forged T-piece. A detailed evaluation of the header can be found in [3,4,30]. Material D was taken from the same section as material C, but this section was subjected to a post-service heat treatment. This heat treatment consisted of renormalization at 1065 °C for 0.5 h, followed by air cooling (AC) and tempering at 775 °C for 1 h again, followed by AC. Finally, material E was sourced from a P91 barrel section of a header retired after 87,000 h operation. Reference [31] provides additional information about the service experience of this header and the subsequent post-service characterization. Some of these materials have a history of service in power-generation plants, but in this study, the initial state of each material is considered to be at the time it was acquired for mechanical testing.

A chemical composition analysis including tramp elements was performed for all the six materials, and the results are summarized in Table 1. The allowable composition ranges specified for ASME SA335 P91 [32] are also listed in this table. In these specifications, Type 1 represents the conventional regulation, while Type 2 represents a new regulation designed to enhance both creep strength and ductility, as explained in the introduction. It is noteworthy that materials C/D and E contain numerous tramp elements, with sulfur (S), copper (Cu), and arsenic (As) exceeding the Type 2 requirements. Additionally, they have a high aluminum (Al) content that does not even comply with Type 1 regulations. In contrast, the remaining three materials demonstrate relatively low impurity levels. In particular, materials A and B meet the Type 2 requirements entirely, while material F does not meet the requirements only in terms of the N/Al ratio.

Table 1. Chemical composition of the Grade 91 parent materials (in mass %) compared to the requirements in ASME SA-335 P91.

Element	A	B	C/D	E	F	ASME SA-335 P91	
						Type 1	Type 2
C	0.10	0.08	0.10	0.08	0.10	0.08~0.12	
Mn	0.44	0.45	0.41	0.41	0.40	0.30~0.60	0.30~0.50
P	0.003	0.015	0.009	0.012	0.012	≤0.020	
S	0.001	<0.001	0.010	0.009	0.002	≤0.010	≤0.005
Si	0.26	0.24	0.41	0.14	0.33	0.20~0.50	0.20~0.40
Cr	8.94	8.43	8.77	8.88	8.30	8.0~9.5	
Mo	0.91	0.87	0.94	0.93	0.94	0.85~1.05	
W	<0.002	<0.002	Not detected	<0.002	Not detected	-	≤0.05
Ni	0.04	0.11	0.12	0.14	0.19	≤0.40	≤0.20
V	0.21	0.20	0.21	0.21	0.21	0.18~0.25	
Nb	0.086	0.072	0.071	0.061	0.070	0.06~0.10	
N	0.0539	0.0429	0.0454	0.0447	0.0424	0.03~0.07	0.035~0.070
Cu	0.01	0.03	0.19	0.18	0.05	-	≤0.10
Al	0.013	0.010	0.040	0.034	0.020	≤0.02	≤0.020
B	<0.0003	0.0003	<0.0003	<0.0010	<0.0003	-	≤0.001
Ti	0.002	0.009	<0.002	0.002	<0.002	≤0.01	
Zr	<0.002	<0.002	<0.002	<0.002	<0.002	≤0.01	

Table 1. *Cont.*

Element	A	B	C/D	E	F	ASME SA-335 P91	
						Type 1	Type 2
As	0.002	0.003	0.013	0.014	0.004	-	≤0.010
Sn	0.001	<0.001	0.008	0.008	0.003	-	≤0.010
Sb	<0.0001	<0.0001	0.0023	0.0019	0.0006	-	≤0.003
N/Al	4.1	4.3	1.1	1.3	2.1	-	≥4.0

2.2. Tensile Test Method

Tensile tests were conducted on the six Grade 91 steels at 625 °C using specimens with a test section diameter of 10 mm and a gauge length of 50 mm, as illustrated in Figure 1. These tests were carried out under strain control, maintaining a constant nominal strain rate of 0.1%/s until rupture occurred. The number of tensile tests for each material was one. An electro-mechanical tensile testing machine (Shimadzu AUTOGRAPH AG-100kN) equipped with an electric furnace was employed for these experiments. The nominal strain of the specimen was measured using two linear variable differential transformer (LVDT)-type extensometers and rods affixed to the ridges machined on the specimens. Specimen temperature was monitored using R-type thermocouples attached to the specimen's surface, maintaining a specified temperature with a precision of ± 3 °C.
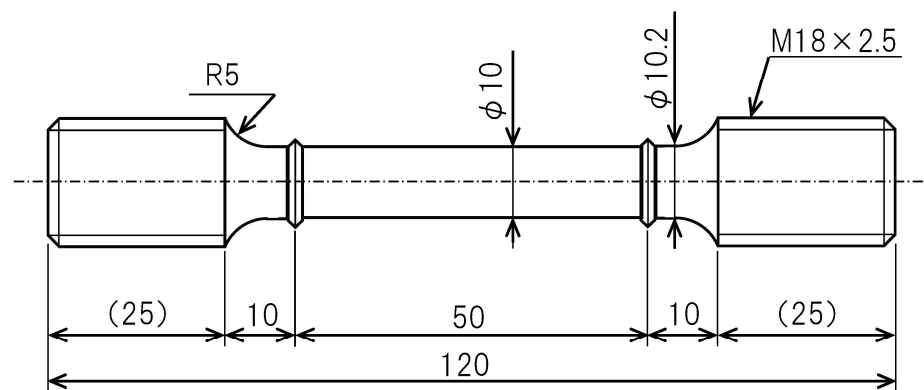

Figure 1. Test specimen used for tensile and creep tests (unit: mm).

2.3. Creep Test Method

Creep tests were conducted using the plain bar specimen shown in Figure 1 under a constant tensile load calculated from the initial diameter of the specimen and the planned stress. Four or five stress levels at 625 °C were applied to each material to evaluate the material difference in creep rupture time and creep rupture ductility. A few tests were also performed at 650 °C for materials C, D, E, and F to assess the temperature-dependence of the creep rupture behavior. For materials A and B, a lot of creep data were obtained at 600 and 650 °C. These test data for material A are reported in [16]. Conventional dead-weight-type creep testing machines with an electrical furnace were employed for all the tests. Elongation of the specimen was continuously measured using two LVDT-type extensometers and rods mounted on the ridges of the specimen. Temperature was measured using R-type thermocouples attached to the specimen and kept at a specified temperature with the precision of ± 2 °C using the electric furnace.

2.4. Fatigue and Creep-Fatigue Test Method

Strain-controlled fatigue and creep-fatigue tests were performed on the six Grade 91 steels. In fatigue tests, the primary conditions were 600 °C, with a total strain range of 1.0% ($\Delta \varepsilon_t = 1.0\%$) and 625 °C with $\Delta \varepsilon_t = 0.5\%$. For creep-fatigue tests, a holding time

of 1 h ($t_H = 1$ h) at the maximum tensile strain was added to the fatigue test conditions mentioned above. Materials B and C were subjected to testing at 625 °C, with a wider total strain range ($\Delta\varepsilon_t = 0.35$, 1.0%) and an intermediate holding time ($t_H = 0.167$ h). Plain bar specimens with test sections of 8 or 10 mm diameter, as shown in Figure 2, were utilized for these tests. Electro-mechanical fatigue testing machines (Instron 8861/8862) equipped with an electrical furnace were employed. Furnace temperatures were controlled using thermocouples built into the furnace, while the specimen's temperature was monitored using a thermocouple attached to the specimen's surface. An extensometer with a 12.5 mm gauge length was mounted on the parallel section of the specimen. Axial load was applied in the strain-control mode following a triangular waveform in the fatigue tests and a trapezoidal waveform with a hold at the tensile peak in the creep-fatigue tests. The strain rate during the fatigue cycle was fixed at 0.1%/s for all tests. Failure was defined as a 25% reduction in maximum stress from the steady state.
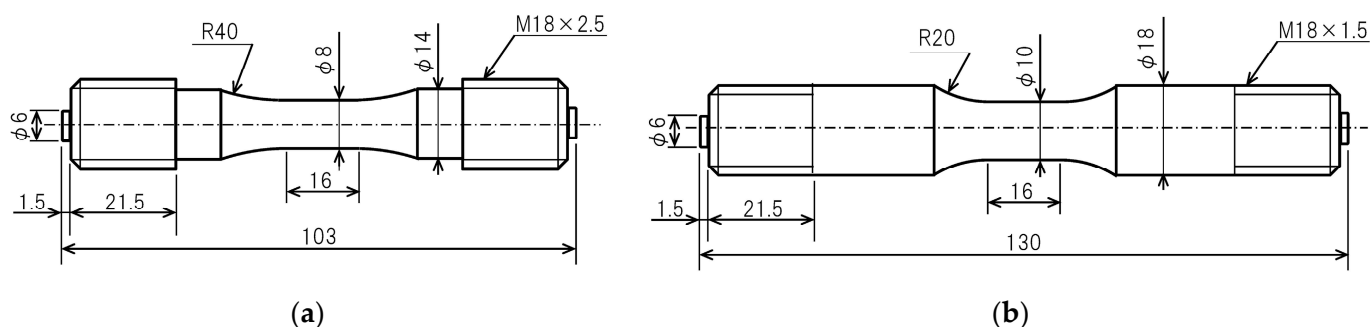

(a)　　　　　　　　　　　　　　　　　　　　　**(b)**

Figure 2. Test specimens used for fatigue and creep-fatigue tests (unit: mm). (**a**) Specimen with 8 mm diameter used in the tests at 625 °C; (**b**) specimen with 10 mm diameter used in the tests at 600 °C.

3. Results and Discussion

3.1. Tensile Properties

Table 2 presents the values of 0.2% proof stress, tensile strength, elongation, and reduction in area obtained in the tensile tests at 625 °C with constant strain rate of 0.1%/s. These results demonstrate good ductility across all heats, with elongation exceeding 30% and reduction in area exceeding 80%. However, significant differences in tensile strength are evident among the six materials, which is visually evident in the comparison of nominal stress–nominal strain curves, as depicted in Figure 3. Material A exhibits the highest strength, followed by D, B, C, and E, while F demonstrates notably lower strength compared to the other materials. These curves are characterized by minimal work hardening under the tested conditions of 625 °C and a strain rate of 0.1%/s, reaching maximum stress at an exceptionally low strain.

Table 2. Summary of tensile test results at 625 °C with constant strain rate of 0.1%/s.

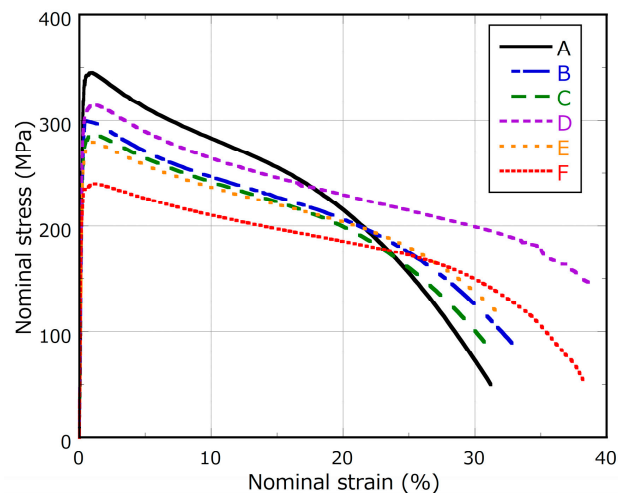| Material	0.2% Proof Stress (MPa)	Tensile Strength (MPa)	Elongation (%)	Reduction in Area (%)
A	341	345	32	95
B	304	306	38	96
C	275	287	32	82
D	301	315	49	89
E	270	280	35	83
F	235	240	41	90

Figure 3. Comparison of nominal stress–nominal strain curves of six heats at 625 °C.

3.2. Creep Properties

Figure 4 plots the rupture time obtained in each creep test at 625 °C as a function of applied stress. Although a portion of these test data was previously reported by the authors [7–9], this figure includes additional long-term creep rupture data. For comparison, the average creep rupture property calculated using the following equation is also depicted in this figure:

$$\log t_{r,ave} = \min \left\{ \begin{array}{l} \left[27140.7 + 12714.9(\log \sigma) - 5079.8(\log \sigma)^2 \right] / T_{abs} - 32.3000 \, , \\ \left[23067.7 + 3744.7(\log \sigma) - 2144.9(\log \sigma)^2 \right] / T_{abs} - 20.6583 \end{array} \right\} , \quad (1)$$

where $t_{r,ave}$ represents the average creep rupture time (in hours) calculated from the applied stress, σ (in MPa), and the absolute temperature, T_{abs} (in K). This equation combines the average property of Grade 91 steel [33] obtained for pipe and forgings in the high-stress regime and that for plate in the low-stress regime. This combination was undertaken to ensure that the curves of the low- and high-stress regions intersect and make it possible to fit the test data just by multiplying heat-dependent constants. However, it is important to note that even with this formula, the two curves do not intersect at high temperatures and that a turnaround point appears in the low-stress region. Therefore, the applicable range of this formula is $T_{abs} \leq 925$ K and $\sigma \geq 20$ MPa. In Figure 4, significant differences in creep strength among the tested materials are evident. Among them, material A exhibits the highest creep strength, surpassing the average trend curve, followed by material B just around the average curve. Materials F and D show similar creep strength, tracking material B. On the other hand, materials C and E exhibit the weakest trends.

Figure 5a shows the variation in creep rupture elongation at 625 °C with rupture time. A significant difference among the tested materials appears again. Materials C and E show similar small elongations, tending to represent the lowest ductility. Material D has slightly higher elongation than them but does not seem to show a good ductility. Eight data points with notably low elongation of these three materials experienced failure at the cross-section adjacent to the ridge for extensometer mounting, probably due to sensitivity to stress triaxiality and/or stress concentration. The other materials generally exhibit high elongations, although the elongation tended to decrease significantly as the rupture time increased in material F. Similar but more pronounced trends can be observed in the reduction in area, as shown in Figure 5b. Here, the behavior may be clearly divided into three groups: a high-level group comprising materials A, B, and F; a low-level group consisting of materials C and E; and a medium-level group consisting solely of material D. Among the high-level group, material F began to deviate at approximately 1000 h from the stable value of over 80%, which was commonly observed in the high-level group, down to

the level of the lowest-ductility group. It can be also seen that relatively high values were obtained at short rupture times even in the low-level group.
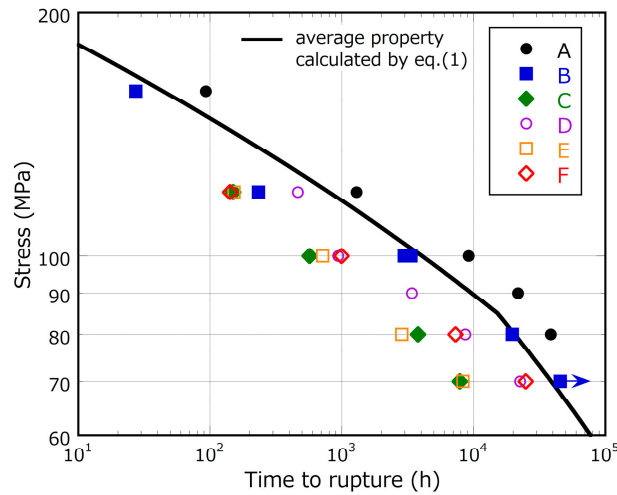

Figure 4. Relationship between stress and time to creep rupture at 625 °C. The line represents the average creep rupture property of Grade 91 steel calculated from Equation (1). One test (material B, 70 MPa) is ongoing.
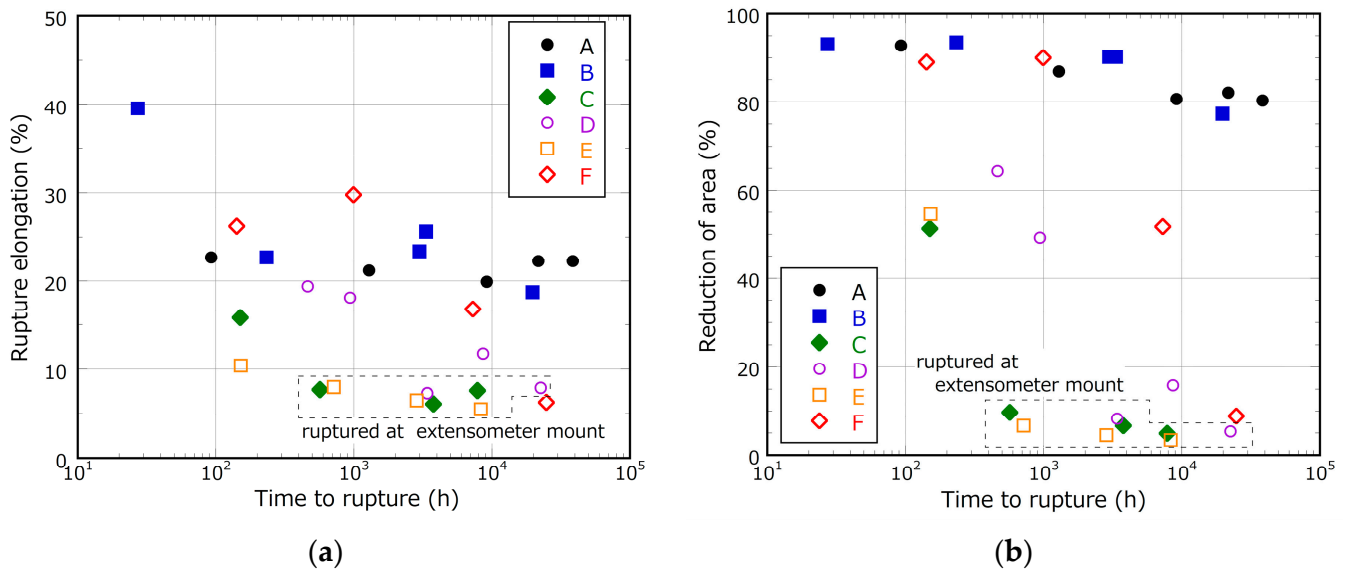

Figure 5. Variation of creep rupture ductility with respect to creep rupture time at 625 °C. (**a**) Rupture elongation; (**b**) reduction in area. Eight data points with particularly small ductility in materials C, D, and E fractured adjacent to the extensometer mount.

Since materials C to F have service experience in power plants, it is not straightforward to compare creep characteristics among all materials. However, it is evident that materials A and B, which satisfy the ASME Type 2 specifications, excelled in both creep life and creep rupture ductility. In the case of materials C and F, with the same service experience, material C, which contains more impurity elements, exhibited significantly shorter creep life and lower creep rupture ductility. Particularly, the fact that material D, which was subjected to re-normalization and tempering for material C to achieve a microstructure equivalent to virgin material, still showed lower creep strength and creep rupture ductility supports the idea that excessive impurity elements adversely affect the creep strength and creep rupture ductility of this steel.

3.3. Fatigue and Creep-Fatige Properties

Figure 6 displays the relationship between total strain range and the number of cycles to failure in strain-controlled fatigue and creep-fatigue tests. In Figure 6a, presenting the results of all materials, the material difference in fatigue lives is smaller compared to the creep-fatigue lives. The creep-fatigue lives of materials A, B, and F exhibited better performance compared to the other three materials. Figure 6b shows a comparison of the number of cycles to failure in materials B and C under various test conditions, including those not included in Figure 6a. The fatigue lives of materials B and C are almost the same, except for the test with a total strain range of 0.35%. The failure life decreased as the hold time increased for both heats, but the degree of decline was more pronounced for material C.
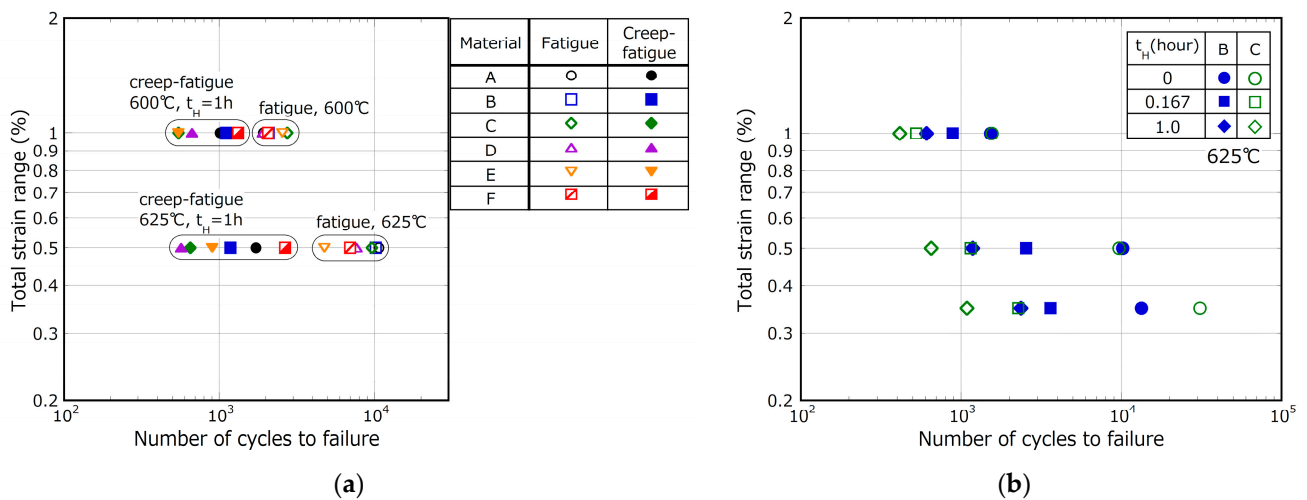

Figure 6. Relationship between total strain range and number of cycles to failure for strain-controlled fatigue and creep-fatigue tests. (**a**) Comparison of failure lives of the six materials; (**b**) comparison of failure life of materials B and C in various strain-range and hold-time conditions.

The relationship between the hold time and the number of cycles to failure is shown in Figure 7. In Figure 7a, it appears that material F experiences less reduction in fatigue life due to strain hold compared to the other materials. The comparison between materials B and C, as shown in Figure 7b, reaffirms that the decrease in life due to tensile strain holding is larger in material C. This may be related to the lower creep strength and creep ductility of material C compared to material B.

Comparisons of changes in tensile and compressive peak stresses with cycles in each test condition are presented in Figure 8. The stress at the end of hold time is also displayed for creep-fatigue tests, shown in Figure 8c,d. In Figure 8d, the peak stresses of materials A, B, and D increase at the end of the test, which indicates that cracks have initiated and grown outside the gage length. In such cases, failure was defined as the point at which the maximum stress started to increase. All materials exhibited qualitatively similar cyclic softening behavior, but stress levels showed some material difference, with the highest observed in material A and the lowest in material F. This material difference was similar to the tensile strength and stress-strain curves observed in tensile tests.

Figure 9 compares the hysteresis loops at half-life cycles for each test condition. The stress range of material F is smaller than that of other materials in all test conditions. This characteristic is particularly noticeable in creep-fatigue tests.

Comparisons of stress-relaxation behavior at half-life cycles in creep-fatigue tests are shown in Figure 10. This figure also clearly shows that material F exhibited lower stress levels compared to the other materials even during stress relaxation.
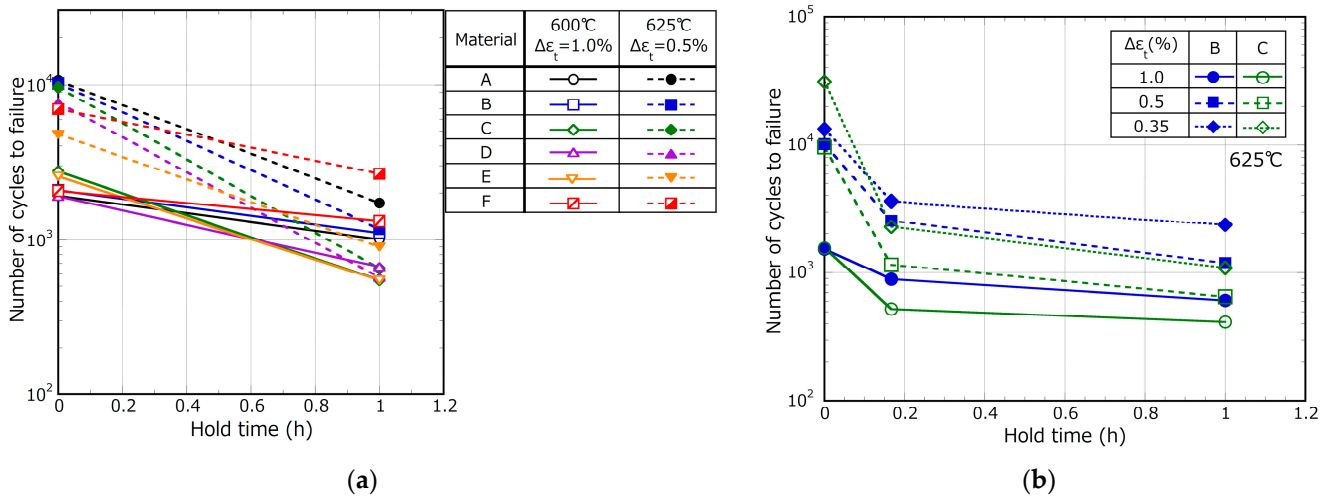
(**a**)

(**b**)

Figure 7. Relationship between number of cycles to failure and hold time. (**a**) Comparison between the six materials under two different conditions; (**b**) comparison between materials B and C under various strain-range and hold-time conditions.

(**a**)

(**b**)
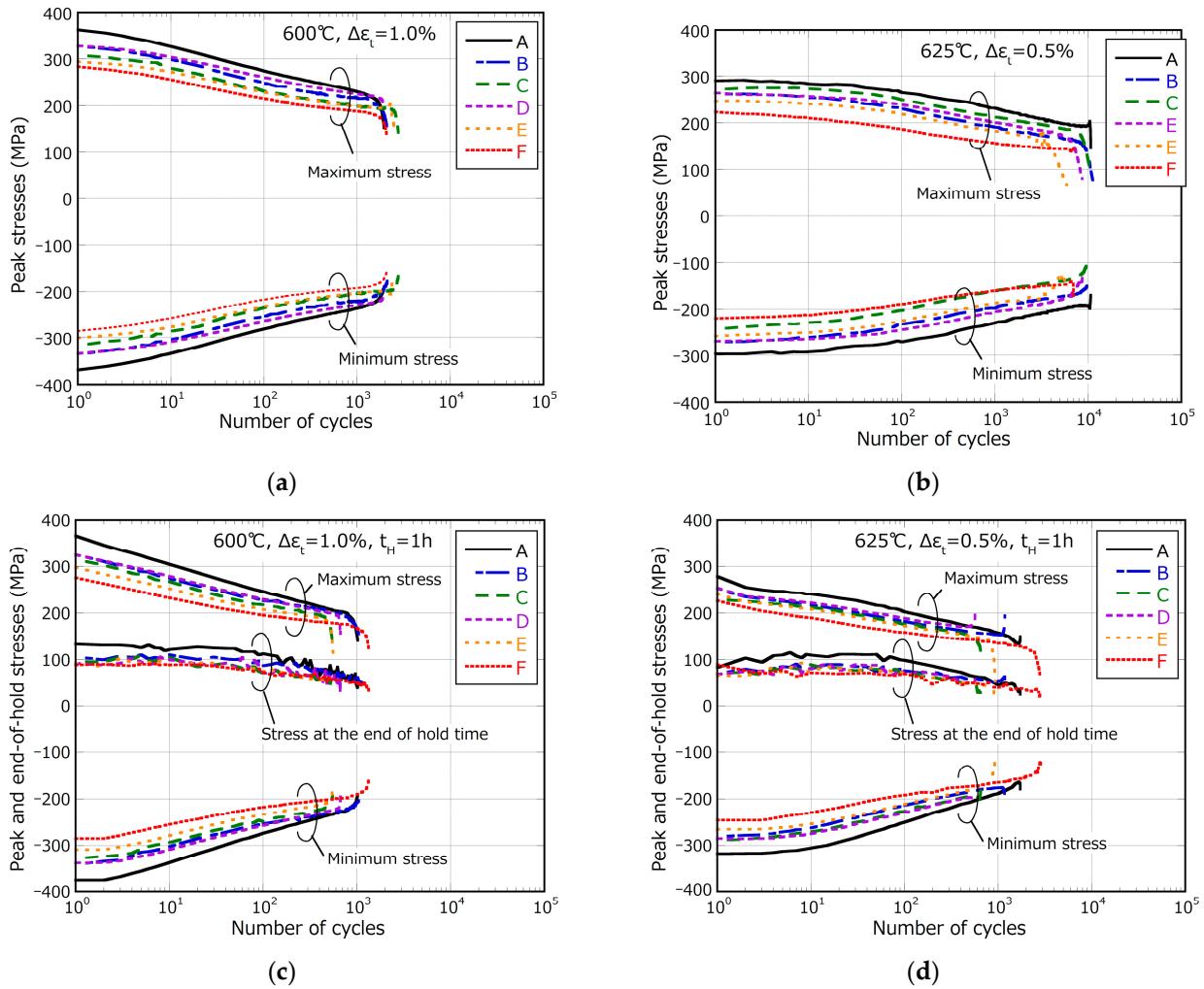

(**c**)

(**d**)

Figure 8. Comparison of change in peak stresses in fatigue and creep-fatigue tests in the six materials. The stress at the end of hold time is also displayed for creep-fatigue tests. (**a**) Fatigue test, 600 °C, $\Delta\varepsilon_t = 1.0\%$; (**b**) fatigue test, 625 °C, $\Delta\varepsilon_t = 0.5\%$; (**c**) creep-fatigue test, 600 °C, $\Delta\varepsilon_t = 1.0\%$, $t_H = 1$ h; (**d**) creep-fatigue test, 625 °C, $\Delta\varepsilon_t = 0.5\%$, $t_H = 1$ h.
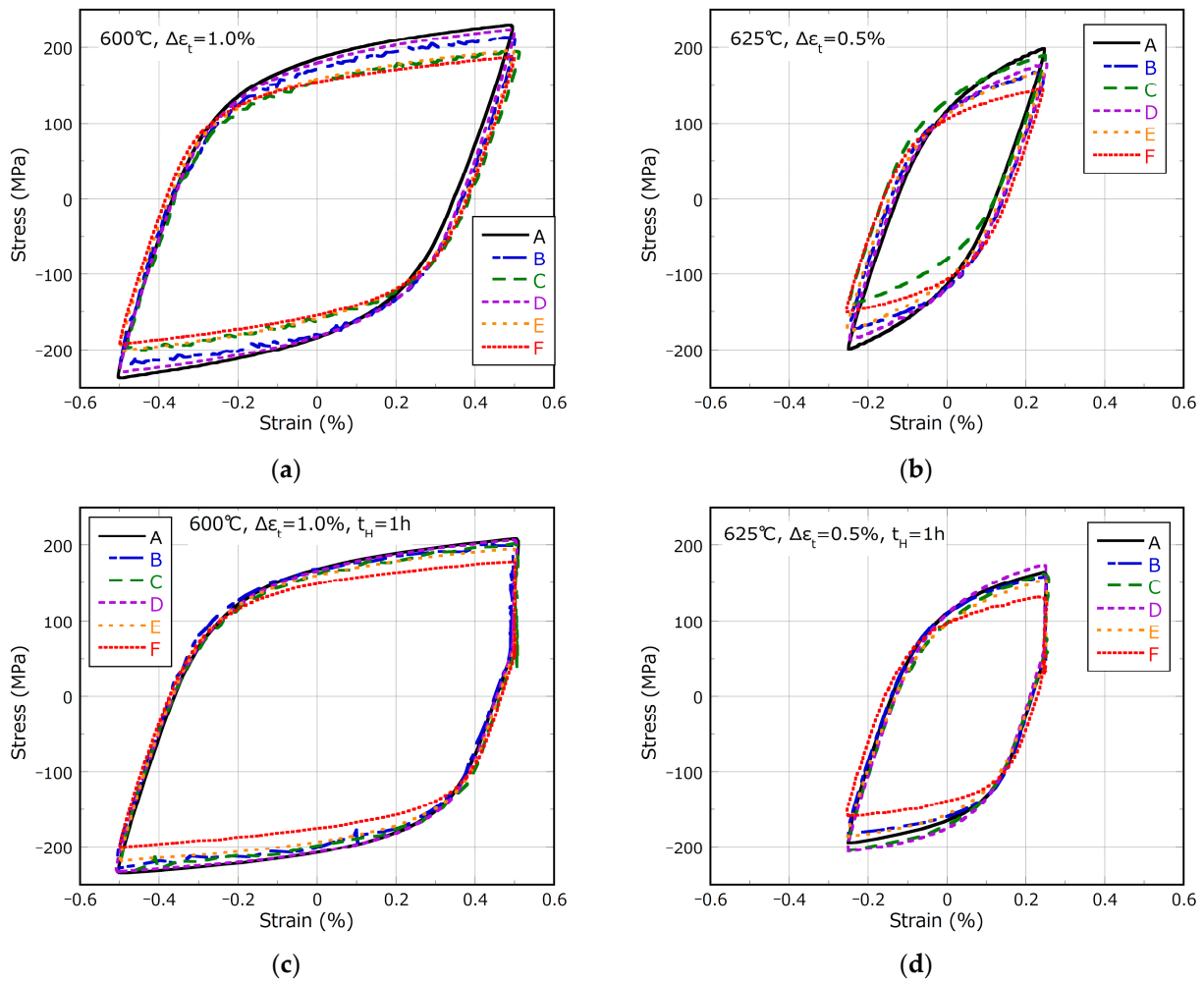
Figure 9. Comparison of hysteresis loops at half-life cycles in fatigue and creep-fatigue tests. (**a**) Fatigue test, 600 °C, $\Delta\varepsilon_t = 1.0\%$; (**b**) fatigue test, 625 °C, $\Delta\varepsilon_t = 0.5\%$; (**c**) creep-fatigue test, 600 °C, $\Delta\varepsilon_t = 1.0\%$, $t_H = 1$ h; (**d**) creep-fatigue test, 625 °C, $\Delta\varepsilon_t = 0.5\%$, $t_H = 1$ h.
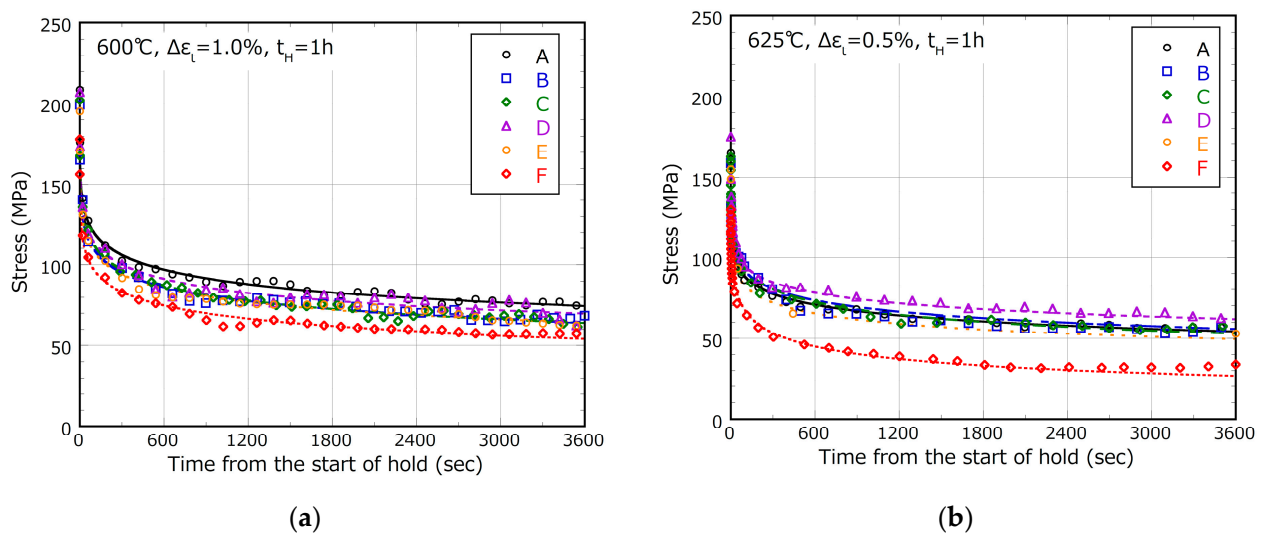

Figure 10. Comparison of stress-relaxation behavior at half-life cycles in creep-fatigue tests. (**a**) 600 °C, $\Delta\varepsilon_t = 1.0\%$, $t_H = 1$ h; (**b**) 625 °C, $\Delta\varepsilon_t = 0.5\%$, $t_H = 1$ h. Each line represents the regression curve given by Equation (3) used for calculating creep damage in creep-fatigue life evaluation.

3.4. Variations in Creep, Fatigue, and Creep-Fatigue Lives

Figure 11 illustrates the comparison of variations in creep, fatigue, and creep-fatigue lives. While some variations are present, the material difference in creep rupture time was well preserved even when stress levels changed. The creep rupture life exhibited significant variations, with a maximum difference of approximately one order of magnitude. On the other hand, material difference in fatigue life was small compared to that of creep life. Creep-fatigue life fell between the two in terms of material difference. Materials A and B, which have excellent creep strength and ductility, had a relatively long life even in 1-h-hold creep-fatigue tests, but material F had the longest creep-fatigue life. This may be related to the fact that material F displayed notably low stress levels during stress relaxation.
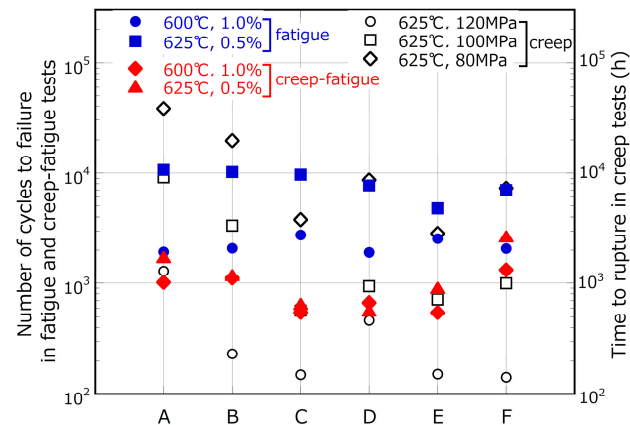

Figure 11. Variations in creep, fatigue, and creep-fatigue lives.

To quantitatively evaluate variations in failure life, the coefficient of variation (*CV*) for each test was calculated using the following equation:

$$CV = s_x / \overline{x} , \tag{2}$$

where s_x represents the standard deviation of life across the six materials for each test condition, and $\overline{x}$ is the average life. Table 3 provides a summary of the coefficient of variation for each test condition, reinforcing the recognition that the variations in fatigue and creep-fatigue life are smaller compared to those observed in creep life. The creep, fatigue, and creep-fatigue test data used for the *CV* calculation are summarized in Appendix B.

Table 3. Coefficient of variation of creep, fatigue, and creep-fatigue lives.

Test Conditions		Coefficient of Variation
Creep	625 °C, 120 MPa	1.015
	625 °C, 100 MPa	1.195
	625 °C, 80 MPa	0.926
Fatigue	600 °C, $\Delta\varepsilon_t = 1.0\%$	0.145
	625 °C, $\Delta\varepsilon_t = 0.5\%$	0.249
Creep-Fatigue	600 °C, $\Delta\varepsilon_t = 1.0\%$, $t_H = 1$ h	0.344
	625 °C, $\Delta\varepsilon_t = 0.5\%$, $t_H = 1$ h	0.566

4. Evaluation of Creep-Fatigue Failure Lives

4.1. Outline of Creep Damage Evaluation Methods

Changes in stress during the hold time are required to calculate creep damage per cycle, d_c, in the creep-fatigue test. To avoid irregular changes of inelastic strain rate due to

small fluctuations of measured stress during stress relaxation, the variation of stress during hold time was approximated by the following function:

$$\sigma = \sigma_0 / (A_r t^{m_r} + 1) \, , \tag{3}$$

where σ_0 and t denote the stress at the start of hold period and the time elapsed after the start of the hold, whereas A_r and m_r are constants used for fitting the data. The fitted stress-relaxation curves at half-life cycles are compared with the experimental data in Figure 10, confirming the accuracy of Equation (3) in simulating the stress-relaxation behavior. The accumulated creep damage, D_c, in the creep-fatigue test was calculated by multiplying the creep damage obtained for the half-life cycles by the number of cycles to failure in the creep-fatigue test, $N_{f,creep-fatigue}$:

$$D_c = d_c N_{f,creep-fatigue} \, . \tag{4}$$

In this paper, the creep damage per cycle is estimated by the following five approaches.

4.1.1. Time Fraction Approach

The time fraction approach considers stress and temperature as the principal parameters governing creep damage progression and calculates creep damage per cycle through time integration according to the following equation, which takes into account the stress variation during the hold time:

$$d_c = \int_0^{t_H} \frac{1}{t_r(\sigma, T_{abs})} dt \, . \tag{5}$$

In this equation, the creep rupture properties of each material, as represented by the following equation, were employed to evaluate time fraction creep damage:

$$t_r = p_0 t_{r,ave} \, , \tag{6}$$

where p_0 is a material-dependent constant, and $t_{r,ave}$ represents the average creep rupture time of Grade 91 steel calculated from Equation (1). The constant p_0 was determined by regression of creep test data at various temperatures, as shown in Table 4. Figure 12 provides a comparison between the creep test data and the creep rupture curves. As mentioned before, Equation (1) is applicable within the range of $T_{abs} \leq 925$ K and $\sigma \geq 20$ MPa. In the creep-fatigue tests performed in this study, the temperature and stress during holding always satisfy these ranges.
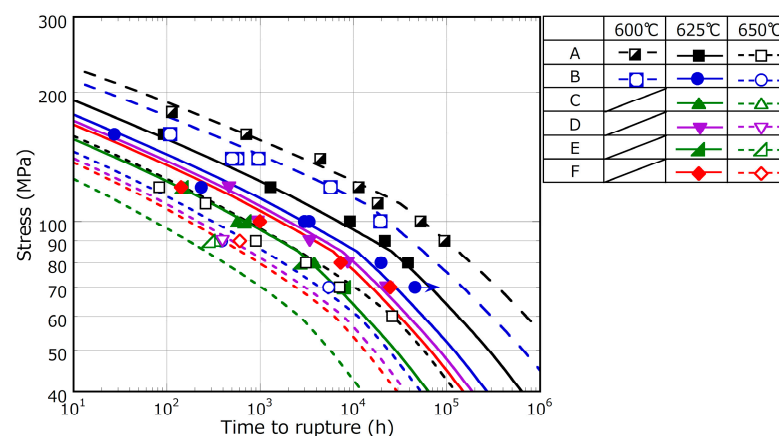

Figure 12. Creep test data at various temperatures and regression curves given by Equation (6) and constants in Table 4. Each creep rupture curve was used in calculation of creep damage for the time fraction approach. Note that the constant p_0 of materials C and E is the same value, so their creep rupture curves are the same.

Table 4. Summary of constants in each creep damage function. The values in this table are valid for stress represented in MPa, inelastic strain rate in/h, inelastic strain energy density at rupture in MJ/m^3, and inelastic strain energy density rate in MJ/m^3 h.

Constants	A	B	C	D	E	F
p_0	1.70	7.20×10^{-1}	1.70×10^{-1}	5.00×10^{-1}	1.70×10^{-1}	4.00×10^{-1}
ε_{f0}	3.24×10^{-1}	3.76×10^{-1}	3.19×10^{-1}	4.85×10^{-1}	3.53×10^{-1}	4.06×10^{-1}
p_1	4.61×10^{-1}	1.06	6.22	1.25×10^1	8.46	3.63×10^1
p_2	2.66×10^{-2}	6.14×10^{-2}	1.70×10^{-1}	1.82×10^{-1}	1.85×10^{-1}	2.15×10^{-1}
W_{f0}	7.23×10^1	6.91×10^1	6.54×10^1	7.81×10^1	6.73×10^1	6.23×10^1
p_3	6.57×10^{-1}	2.61×10^{-1}	4.06×10^{-3}	3.73×10^{-3}	3.60×10^{-3}	3.45×10^{-3}
p_4	1.21×10^{-1}	1.48×10^{-1}	2.56×10^{-1}	2.73×10^{-1}	2.58×10^{-1}	2.83×10^{-1}
p_5	4.17×10^{-1}	1.65×10^{-1}	1.45×10^{-3}	1.34×10^{-3}	1.23×10^{-3}	1.41×10^{-3}
p_6	1.35×10^{-1}	1.61×10^{-1}	2.85×10^{-1}	3.02×10^{-1}	2.88×10^{-1}	3.07×10^{-1}

4.1.2. Ductility Exhaustion Approach

According to the classical ductility exhaustion approach [15], creep damage per cycle was calculated based on the inelastic strain rate, $\dot{\varepsilon}_{in}$, and temperature as follows:

$$d_c = \int_0^{t_H} \frac{\dot{\varepsilon}_{in}}{\varepsilon_f\left(\dot{\varepsilon}_{in}, T_{abs}\right)} dt , \qquad (7)$$

where ε_f represents the limit of strain that the material can endure, known as rupture ductility. Various quantities such as rupture elongation, reduction of area, and true rupture strain obtained in creep tests have been used for its determination, depending on researchers and/or materials. Here, values of rupture elongation obtained in the creep tests were formulated as a function of inelastic strain rate–temperature parameter, Ω, to be used as the ductility:

$$\Omega = \dot{\varepsilon}_{in} \exp(Q/RT_{abs}), \qquad (8)$$

where Q is an activation energy, and R is the gas constant (8.314 J/mol/K). Figure 13 shows the relationship between rupture ductility and the inelastic strain rate–temperature parameter. Here, the average strain rate calculated by dividing the creep rupture elongation by the creep rupture time was used, although the strain rate changes with time in creep tests. The activation energy value was set to -1.16×10^5 J/mol based on the creep database of the National Institute for Materials Science (NIMS) [34], which includes various heats and temperatures data. See Appendix A for the derivation of the activation energy. The negative value of the activation energy indicates that the change of rupture elongation is not governed by thermal activation only, and the involvement of other factors such as stress is suggested, but this value was simply applied for describing the temperature dependency of rupture elongation in an empirical way. Data from the plain bar creep tests were fitted with power-law functions, which were used in conjunction with an upper bound value, ε_{f0}, obtained from strain-controlled tensile tests performed at 625 °C and the average strain rate of 0.1%/s, as follows:

$$\varepsilon_f = \min\left(\varepsilon_{f0}, p_1\Omega^{p_2}\right). \qquad (9)$$

The constants ε_{f0}, p_1, and p_2 for each material are summarized in Table 4, and the results of the modeling are also presented in Figure 13 with the test data. The inelastic strain rate during strain holding in the creep-fatigue test was calculated by the following:

$$\dot{\varepsilon}_{in} = \dot{\sigma}/E , \qquad (10)$$

where $\dot{\sigma}$ is the rate of stress change, and E is Young's modulus (168,000 MPa for 600 °C and 164,500 MPa for 625 °C).
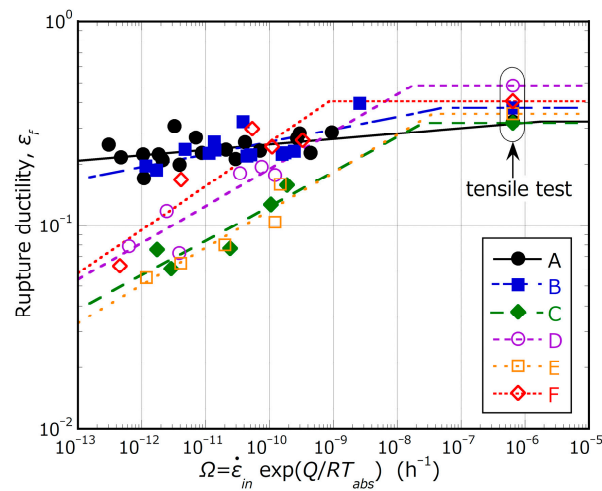
Figure 13. Relationship between rupture ductility and inelastic strain rate–temperature parameter. Each line was employed in the calculation of creep damage for both the ductility exhaustion and modified ductility exhaustion approaches. The value of the activation energy was set to -1.16×10^5 J/mol based on the NIMS creep database, which includes various heat and temperature data.

4.1.3. Modified Ductility Exhaustion Approach

To improve the predictability of the classical ductility exhaustion approach, a new model was developed to estimate creep damage by redefining creep damage as the amount of ductility loss relative to the ductility exhibited in the absence of creep damage [16]. The formula is as follows:

$$d_c = \int_0^{t_H} \left(\frac{1}{\varepsilon_f\left(\dot{\varepsilon}_{in}, T_{abs}\right)} - \frac{1}{\varepsilon_{f0}} \right) \dot{\varepsilon}_{in} dt \ . \tag{11}$$

It should be noted that this equation always yields smaller creep damage than the classical ductility exhaustion approach without a second term. Additionally, it estimates no creep damage when the reduction in ductility does not accompany an increase in creep rupture time. Therefore, the modified approach distinguishes between creep damage leading to a reduction in ductility and simple creep deformation.

4.1.4. Energy-Based Approach

Inelastic strain energy per unit volume accumulated or consumed until rupture might be a more appropriate parameter for characterizing the deformation capability of the material. Actually, several creep-fatigue life evaluation methods based on inelastic strain energy have been developed [18–27]. Here, a similar treatment as made in the modified ductility exhaustion approach led to the following equation [19]:

$$d_c = \int_0^{t_H} \left(\frac{1}{W_f\left(\dot{W}_{in}, T_{abs}\right)} - \frac{1}{W_{f0}} \right) \dot{W}_{in} dt \ , \tag{12}$$

where $\dot{W}_{in}$ is the inelastic strain energy density rate, W_f is the inelastic strain energy density at rupture, and W_{f0} is the upper limit of W_f obtained under sufficiently fast loading. In creep tests, $\dot{W}_{in}$ and W_f can be simply expressed as the inelastic strain rate or rupture ductility multiplied by the applied stress:

$$\dot{W}_{in} = \sigma \dot{\varepsilon}_{in} \ , \tag{13}$$

$$W_f = \sigma \varepsilon_f \ . \tag{14}$$

This method employs inelastic strain energy density instead of inelastic strain as a driving force of creep damage, but it is similar to the above modified ductility exhaustion approach in that the reduction in inelastic strain energy density is considered as creep damage. Figure 14 shows the relationship between inelastic strain energy density at rupture and inelastic strain energy density rate–temperature parameter, Φ, calculated by the following equation:

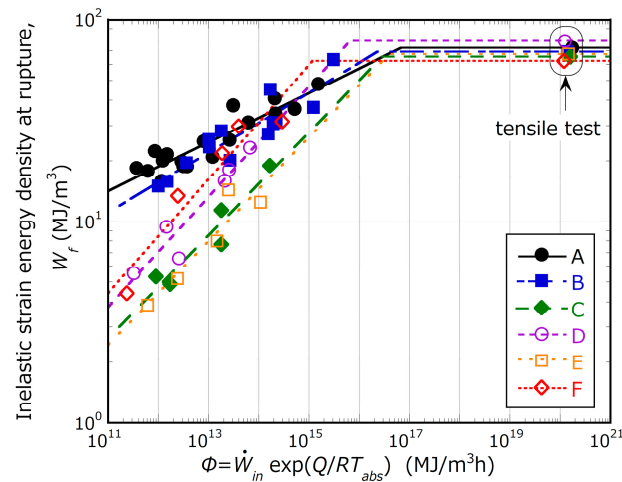$$\Phi = \dot{W}_{in} \exp(Q/RT_{abs}). \tag{15}$$

Figure 14. Relationship between inelastic strain energy density at rupture and inelastic strain energy density rate–temperature parameter. Each line was used in calculation of creep damage for the energy-based approach. The value of activation energy was set as 2.60×10^5 J/mol using the NIMS creep database [34] including various heat and temperature data.

Here, the average value of inelastic strain energy density rate, obtained by multiplying the average strain rate by stress, was used. The activation energy value was set to 2.60×10^5 J/mol based on the NIMS creep database [34], which includes various heat and temperature data. See Appendix A for the derivation of the activation energy. Inelastic strain energy density at rupture for the plain bar creep tests was also regressed using power-law functions, which were used along with an upper-bound value obtained in strain-controlled tensile tests at 625 °C as follows:

$$W_f = \min\left(W_{f0}, p_3 \Phi^{p_4}\right), \tag{16}$$

Constants W_{f0}, p_3, and p_4 of each material are summarized in Table 4, and the comparison of the modeling and original test data is given in Figure 14.

4.1.5. Hybrid Approach

It is considered that the inelastic strain energy density might be a better parameter to describe the effect of creep damage, but its reduction can be regarded as being controlled by inelastic strain rate rather than by inelastic strain energy density rate. Such a concept has been proposed as a hybrid approach [28,29]. It was shown by one of the authors that the stress-modified ductility exhaustion approach proposed by Spindler [35] shares similarities with the hybrid approach [36]. In this paper, creep damage by the hybrid approach was calculated using the following equation:

$$d_c = \int_0^{t_H} \left(\frac{1}{W_f\left(\dot{\varepsilon}_{in}, T_{abs}\right)} - \frac{1}{W_{f0}} \right) \dot{W}_{in} dt, \tag{17}$$

where W_f is the inelastic strain energy density at rupture as in the former approach, but now, it is regarded as a function of the inelastic strain rate rather than that of inelastic strain energy density rate. Figure 15 illustrates the relationship between the inelastic strain energy density at rupture and inelastic strain rate–temperature parameter. The activation energy value was set to 2.98×10^5 J/mol based on the NIMS creep database [34], as shown in Appendix A. Again, the relationships of all materials were approximated by the following:

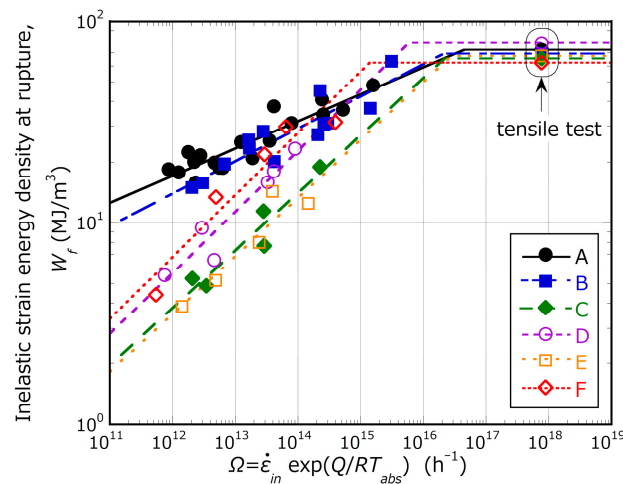$$W_f = \min\left(W_{f0}, p_5\Omega^{p_6}\right). \tag{18}$$

Figure 15. Relationship between inelastic strain energy density at rupture and strain rate–temperature parameter. Each line was used in calculation of creep damage for the hybrid approach. The value of activation energy was set as 2.98×10^5 J/mol using the NIMS creep database including various heat and temperature data.

The constants p_5 and p_6 of each material are summarized in Table 4, and their validity can be seen in Figure 15.

4.2. Outline of Fatigue Damage Evaluation Method

Fatigue damage per cycle, d_f, in the creep-fatigue test was simply calculated as a reciprocal of the fatigue failure life, $N_{f,fatigue}$, at the same total strain range and temperature as in the creep-fatigue test to be evaluated:

$$d_f = \frac{1}{N_{f,fatigue}(\Delta\varepsilon_t, T_{abs})}. \tag{19}$$

The accumulated fatigue damage, D_f, in the creep-fatigue test was calculated by multiplying the fatigue damage by the number of cycles to failure in the creep-fatigue test:

$$D_f = d_f N_{f,creep-fatigue}. \tag{20}$$

4.3. Evaluation of Creep-Fatigue Failure Life

The commonly applied equation to predict creep-fatigue failure lives, assuming linear damage summation, is given by:

$$N_{f,creep-fatigue} = \frac{1}{d_f + d_c}. \tag{21}$$

However, it has been found that failure often occurs earlier than estimated by Equation (21), especially when the creep damage is evaluated using the time fraction approach. An interaction diagram which provides the combination of fatigue dam-

age and creep damage bringing about failure was used in the ASME BPVC Section III Division 5 [14] for design of high temperature nuclear power components to cope with this problem. The current interaction diagram has several choices to apply for different materials. All of them are represented by two linear segments but with different intersection points. When the values of fatigue damage and creep damage at the intersection point are represented by $\overline{D}_f$ and $\overline{D}_c$, the number of cycles to failure can be calculated by the following equation:

$$
N_{f,creep-fatigue} = \begin{cases} \frac{\overline{D}_c}{\overline{D}_c d_f + (1-\overline{D}_f) d_c} \, \text{if} \, \frac{d_f}{d_c} \geq \frac{\overline{D}_f}{\overline{D}_c} \\ \frac{\overline{D}_f}{\overline{D}_f d_c + (1-\overline{D}_c) d_f} \, \text{if} \, \frac{d_f}{d_c} < \frac{\overline{D}_f}{\overline{D}_c} \end{cases} ,
\tag{22}
$$

In addition to the simplest equation based on the assumption that damage can be linearly summed (i.e., Equation (21)), Equation (22) with $\overline{D}_f = 0.1$ and $\overline{D}_c = 0.01$, which is recommended to use for Grade 91 steel in the ASME code was applied in the case of the time fraction approach.

4.4. Results of Damage Calculation and Creep-Fatigue Life Evaluation

Creep and fatigue damage accumulated until failure in creep-fatigue tests are shown in Figure 16a–e for each creep damage evaluation approach. Additionally, a comparison between the five approaches is presented in Figure 16f. The values of creep damage calculated using the time fraction approach are significantly smaller than those required to satisfy the relation $D_f + D_c = 1$ for all test data. The limit provided in the ASME code seems to generally serve as a lower bound for these values, although some data for Materials C and D at 625 °C fall below this limit. Specifically, the three data points below the ASME envelope for Material C are ($\Delta\varepsilon_t = 0.35\%$, $t_H = 1$ h), ($\Delta\varepsilon_t = 0.35\%$, $t_H = 0.167$ h), and ($\Delta\varepsilon_t = 0.5\%$, $t_H = 1$ h). That is, when the total strain range is smaller and the holding time is longer, it is more likely to fall below the ASME envelope. For Material B, which has better creep strength and ductility than Material C, all data are above the ASME envelope, but it may fall below the envelope for lower total strain range and/or longer holding time conditions than those employed in this study. Values of accumulated creep damage evaluated using the classical ductility exhaustion approach are considerably larger and far exceed the line of $D_f + D_c = 1$ for all test data. Values of creep damage calculated by the other three approaches fall between these two extremes, and the data points approach the line representing the linear damage criterion, i.e., $D_f + D_c = 1$. From Figure 16f, it is confirmed that the energy-based and hybrid approaches, in particular, provide closer agreement with the linear damage failure criterion. Although the differences between these two approaches are not significant, there is a tendency for the energy-based approach to yield slightly higher creep damage, resulting in a more conservative evaluation.

Figure 17 presents a comparison of the predictive performance of creep-fatigue lives between the five approaches. The failure lives predicted by the time fraction approach with the linear damage criterion, $D_f + D_c = 1$, are overestimated in all cases, up to a factor of 10. On the other hand, the predicted failure cycles calculated by the time fraction approach with the ASME damage envelope are shorter than the experimental results in most cases. The classical ductility exhaustion approach exhibits a strong tendency to underpredict the failure life, and this tendency increases with an increase in the number of cycles to failure. The underprediction can be up to a factor of 5 for the data obtained in the present study. Agreement with the test data is considerably improved in the modified ductility exhaustion approach compared to the classical ductility exhaustion approach. The energy-based and hybrid approaches can also predict creep-fatigue life effectively. All of the latter three approaches can predict creep-fatigue life almost within a factor of 2.
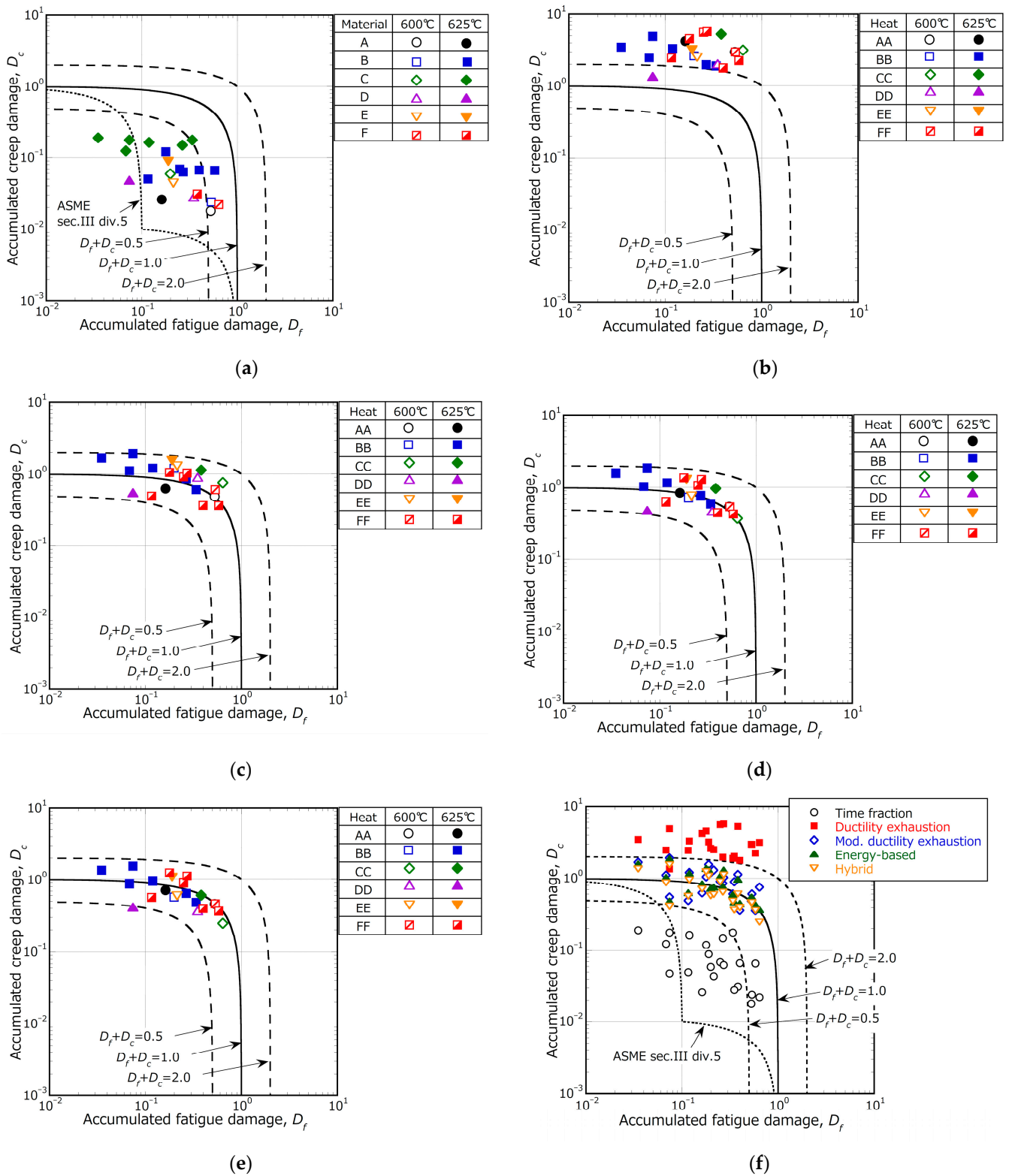
Figure 16. Accumulated creep-fatigue damage diagrams in each approach. (**a**) Time fraction approach; (**b**) Ductility exhaustion approach; (**c**) Modified ductility exhaustion approach; (**d**) Energy-based approach; (**e**) Hybrid approach; (**f**) Comparison between the five approaches. The line through $(D_f = 0.1, D_c = 0.01)$ in (**a**,**f**) is used in the ASME BPVC Section III Division 5 as the creep-fatigue damage envelope for Grade 91 steel in the time fraction approach.
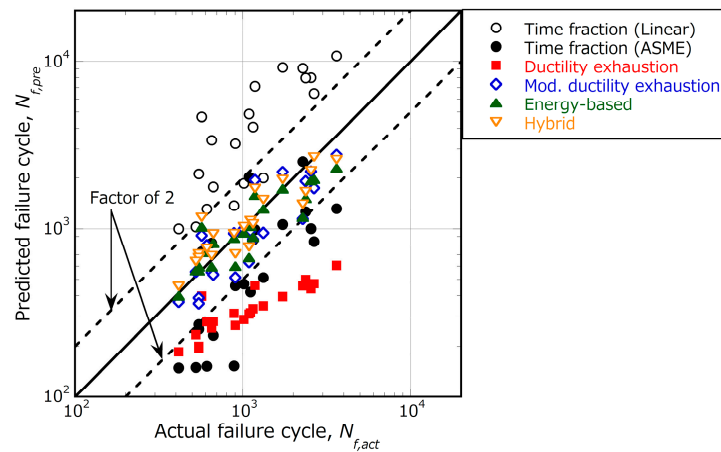
Figure 17. Comparison of performance of five approaches in creep-fatigue life estimation. In the time fraction approach, life evaluation results are shown for the cases using the simple linear damage summation rule ($D_f + D_c = 1$) and the ASME creep-fatigue damage envelope.

To quantitatively assess the prediction accuracy of creep-fatigue life, logarithmic error (*LE*) and root mean squared logarithmic error (*RMSLE*) were calculated for each approach using the following equations:

$$LE = \log\left(N_{f,pre}\right) - \log\left(N_{f,act}\right),$$

(23)

$$RMSLE = \sqrt{\frac{1}{n}\sum_{i=1}^{n}(LE)^2},$$

(24)

where, $N_{f,pre}$ is the predicted life and $N_{f,act}$ is the actual life. n represents the number of tests, and in this case, it pertains to a total of 22 creep-fatigue test data. Figure 18 displays a boxplot of *LE* for each approach. In this figure, a positive LE indicates a non-conservative prediction, while a negative *LE* suggests a conservative prediction. Additionally, the value within the box represents the *RMSLE*, with smaller values indicating better prediction accuracy for the approach. Although the modified ductility exhaustion, energy-based and hybrid approaches all show good prediction accuracy, the hybrid approach is considered to provide the best prediction accuracy in an overall sense.
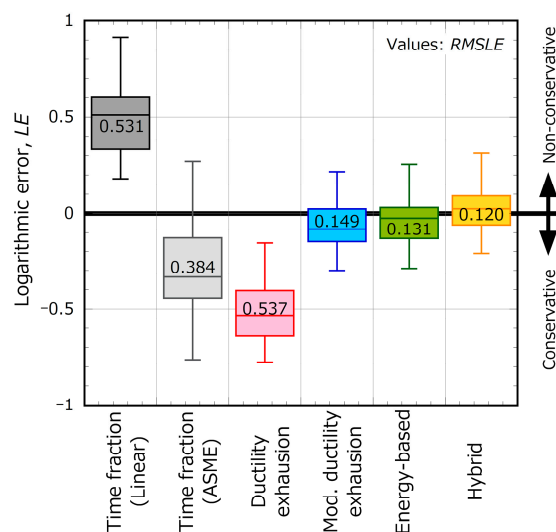

Figure 18. Boxplot of logarithmic error for creep-fatigue life evaluation in each approach. Value in each box shows root mean squared logarithmic error calculated by Equation (24).

5. Conclusions

To investigate the material difference in creep-fatigue properties of Grade 91 steel, a series of tests, including tensile tests, creep tests, strain-controlled fatigue tests, and strain-controlled creep-fatigue tests, were conducted on six Grade 91 steels with different heats and/or histories. The creep rupture lives of the six materials showed differences of more than one order of magnitude under the same test conditions, and the creep rupture ductility also displayed a significant material difference. Nevertheless, the material difference in strain-controlled fatigue life tended to be clearly smaller than that of creep rupture life, and no significant correlation was observed between these lives. On the other hand, a certain degree of correlation was confirmed between the creep-fatigue and creep rupture lives, with the trend that materials exhibiting excellent creep strength and ductility generally demonstrated better creep-fatigue life performance. It should be noted that the creep-fatigue life seemed to be influenced not only by the creep characteristics but also by the stress level during stress relaxation. Furthermore, the material difference in the stress level during stress relaxation also correlated with that of the tensile strength and stress-strain curve obtained in the tensile tests.

The failure life of each creep-fatigue test was predicted using five different approaches of creep damage estimation: time fraction approach, ductility exhaustion approach, modified ductility exhaustion approach, energy-based approach, and hybrid approach. The predictions were based on the stress-relaxation data measured in the creep-fatigue tests and creep rupture properties tailored to each material. The time fraction approach with the creep-fatigue envelope recommended in the ASME code tended to result in non-conservative predictions under conditions of small strain ranges and long holding times. This tendency was more pronounced for materials characterized by low creep strength and ductility. In contrast, the modified ductility exhaustion, energy-based, and hybrid approaches displayed much better prediction accuracy across all materials. Among these three approaches, the hybrid approach demonstrated the highest performance in the statistical analysis on the difference between actual lives and predicted lives. That is to say, the inelastic strain energy density, which can account for the influence of both inelastic strain and stress, is an effective indicator for describing creep damage. In addition, creep-fatigue life can be accurately predicted by considering that the critical value of inelastic strain energy density is controlled by the inelastic strain rate. It might be useful to add, finally, that these findings are quite similar to those previously obtained under three heats on welded joints of Grade 92 steel [28], indicating their generality.

Author Contributions: Conceptualization, H.S., Y.T., J.S., and J.P.; methodology, H.S. and Y.T.; validation, H.S. and Y.T.; formal analysis, H.S.; investigation, H.S. and J.S.; resources, H.S., Y.T., J.S., and J.P.; data curation, H.S.; writing—original draft preparation, H.S.; writing—review and editing, Y.T., J.S., and J.P.; visualization, H.S.; supervision, Y.T. and J.P.; project administration, H.S. and J.S.; funding acquisition, H.S. and J.S. All authors have read and agreed to the published version of the manuscript.

Conflicts of Interest: The authors declare no conflict of interest.

Appendix A

This appendix describes the determination of activation energy values for failure criteria in ductility exhaustion, energy-based, and hybrid approaches. In this research, a comprehensive dataset for deriving the activation energy, i.e., temperature dependence, of individual failure criteria was unavailable. Consequently, the NIMS creep database [34] was employed to obtain these values. The database reports test data for 11 heats of Grade 91 steel over a wide range of temperatures from 500 °C to 725 °C.

Creep rupture ductility, which is the failure criterion in the ductility exhaustion approach, is expressed by the following formula:

$$\ln\left(\varepsilon_f\right) = a_0 + a_1\ln(\dot{\varepsilon}_{in}) + \frac{a_2}{RT_{abs}} \, . \tag{A1}$$

The relationship between creep rupture ductility and creep strain rate at representative temperatures in the database is displayed in Figure A1. Here, the creep rupture elongation and the average creep strain rate, calculated by dividing the creep rupture elongation by the creep rupture time, were employed as the creep rupture ductility and creep strain rate, respectively. Although there is a large variation, and it is not possible to find a clear temperature dependence at a glance, the three constants a_0, a_1, and a_2 in Equation (A1) can be determined by regressing all available data, as shown in Table A1. Similarly, the critical inelastic strain energy density, which is the failure criterion for energy-based and hybrid approaches, is expressed by Equations (A2) and (A3), respectively.

$$\ln\left(W_f\right) = a_0 + a_1\ln\left(\dot{W}_{in}\right) + \frac{a_2}{RT_{abs}} \, , \tag{A2}$$

$$\ln\left(W_f\right) = a_0 + a_1\ln(\dot{\varepsilon}_{in}) + \frac{a_2}{RT_{abs}} \, . \tag{A3}$$

The relationship between inelastic strain energy density at rupture and inelastic strain energy density rate as well as creep strain rate are shown in Figures A2 and A3, respectively. These datasets do not exhibit as much variability as the relationship between creep rupture ductility and creep strain rate shown in Figure A1, and a clear temperature dependence can be seen. The constants in these equations, derived through these regression analyses, are presented in Table A1.

Finally, the activation energy for each failure criterion was calculated by the following:

$$Q = a_2/a_1 \, . \tag{A4}$$

Then, the activation energy values for the failure criteria in the ductility exhaustion, energy-based, and hybrid approaches were determined as -1.16×10^5, 2.60×10^5, and 2.98×10^5 J/mol, respectively. It might be useful to add that the last two values are similar to the activation energy of vacancy diffusion in BCC iron and some ferritic steels, which suggests that the inelastic strain energy density at rupture is governed by the activation of the diffusion. On the other hand, the negative value of the activation energy and larger data scattering in the case of rupture elongation clearly suggest that the ductility is not simply governed by diffusion rate but is also influenced by other factors such as the stress, as systematically investigated in [37].

Table A1. Summary of constants obtained in the regressions for each criterion. The values in this table are valid for inelastic strain rate in /h, inelastic strain energy density at rupture in MJ/m^3, and inelastic strain energy density rate in MJ/m^3 h.

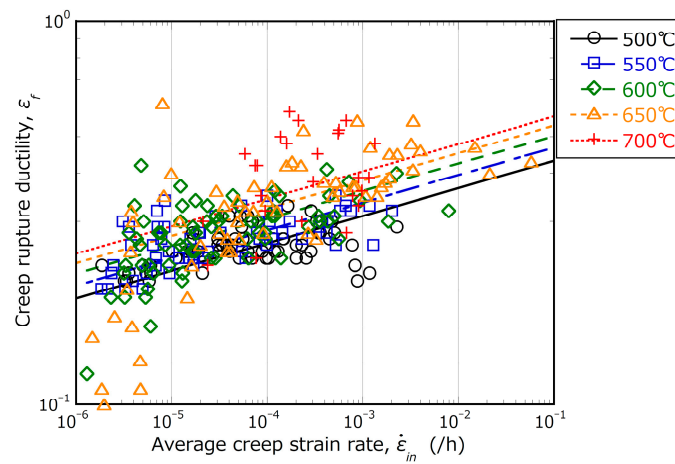| Equation/Approach	a_0	a_1	a_2
(1A)/Ductility Exhaustion	6.26×10^{-1}	7.19×10^{-2}	-8.35×10^3
(2A)/Energy-Based	-1.12	1.50×10^{-1}	3.91×10^4
(3A)/Hybrid	-1.45	1.59×10^{-1}	4.73×10^4

Figure A1. Relationship between creep rupture ductility and creep strain rate at representative temperatures in the NIMS creep database. Each line represents a regression line given by Equation (A1) and constants given in Table A1.
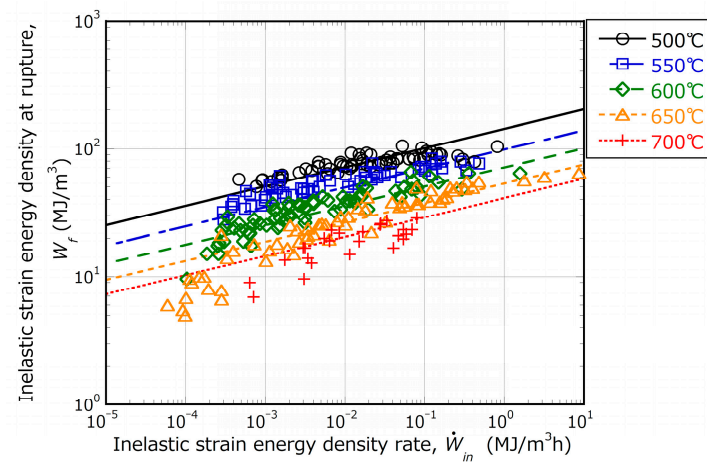

Figure A2. Relationship between inelastic strain energy density at rupture and inelastic strain energy density rate at representative temperatures in the NIMS creep database. Each line represents a regression line given by Equation (A2) and constants given in Table A1.
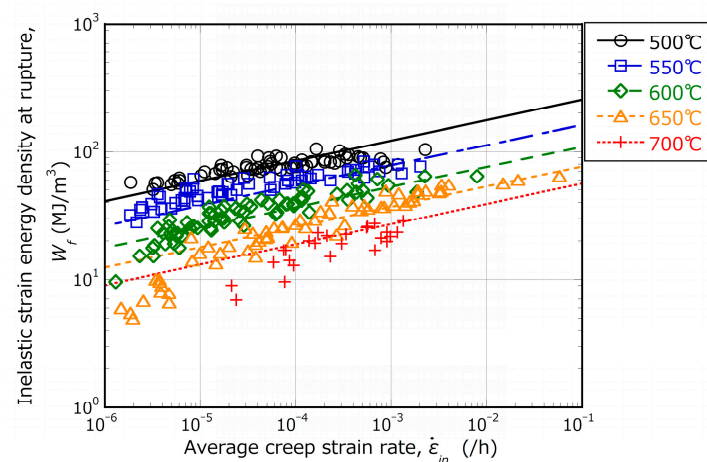

Figure A3. Relationship between inelastic strain energy density at rupture and creep strain rate at representative temperatures in the NIMS creep database. Each line represents a regression line given by Equation (A3) and constants given in Table A1.

Appendix B

The creep, fatigue, and creep-fatigue test data used in the *CV* calculations are summarized in Tables A2–A4.

Table A2. Creep rupture times (hours) of each material used in the *CV* calculations.

Test Conditions	A	B	C	D	E	F
625 °C, 120 MPa	1289.7	233.3	150.3	463.2	152.0	142.1
625 °C, 100 MPa	9159.1	3341.8	568.8	939.0	715.8	994.2
625 °C, 80 MPa	38,440.0	19,703.0	3780.0	8642.8	2852.6	7291.5

Table A3. Fatigue failure lives (cycles) of each material used in the *CV* calculations.

Test Conditions	A	B	C	D	E	F
600 °C, $\Delta\varepsilon_t = 1.0\%$	1930	2090	2750	1910	2560	2070
625 °C, $\Delta\varepsilon_t = 0.5\%$	1010	1110	547	668	546	1320

Table A4. Creep-fatigue failure lives (cycles) of each material used in the *CV* calculations.

Test Conditions	A	B	C	D	E	F
600 °C, $\Delta\varepsilon_t = 1.0\%$, $t_H = 1$ h	10,700	10,200	9660	7690	4770	6980
625 °C, $\Delta\varepsilon_t = 0.5\%$, $t_H = 1$ h	1730	1180	653	569	902	2660

References

1. Kimura, K.; Sawada, K.; Kushima, H.; Toda, Y. Microstructural stability and long term creep strength of Grade 91 steel. *Mater. Sci. Eng. Energy Syst.* **2009**, *4*, 176–183. [CrossRef]
2. Kimura, K.; Sawada, K.; Kushima, H.; Toda, Y. Influence of Chemical Composition and Heat Treatment on Long-term Creep Strength of Grade 91 Steel. *Procedia Eng.* **2013**, *55*, 2–9. [CrossRef]
3. Parker, J.; Brett, S. Creep performance of a Grade 91 header. *Int. J. Press. Vessel. Pip.* **2013**, *111–112*, 82–88. [CrossRef]
4. EPRI. *The Benefits of Improved Control of Composition of Creep-Strength-Enhanced Ferritic Steel Grade 91*; EPRI: Palo Alto, CA, USA, 2014; p. 3002003472.
5. Sawada, K.; Kushima, H.; Hara, T.; Tabuchi, M.; Kimura, K. Heat-to-heat variation of creep strength and long-term stability of microstructure in Grade 91 steels. *Mater. Sci. Eng. A* **2014**, *597*, 164–170. [CrossRef]
6. Maruyama, K.; Nakamura, J.; Sekido, N.; Yoshimi, K. Causes of heat-to-heat variation of creep strength in Grade 91 steel. *Mater. Sci. Eng. A* **2017**, *696*, 104–112. [CrossRef]
7. Takahashi, Y.; Shigeyama, H.; Siefert, J.; Parker, J. Effect of simulated heat affected zone thermal cycle on the creep deformation and damage response of Grade 91 steel including heat-to-heat variation. In Proceedings of the ASME 2018 Pressure Vessels and Piping Division Conference, Prague, Czech Republic, 15–20 July 2018; p. PVP2018-82105.
8. Shigeyama, H.; Takahashi, Y.; Siefert, J.; Parker, J. Creep Deformation Analyses for Grade 91 Steels Considering Heat-to-Heat Variation. In Proceedings of the ASME 2018 Pressure Vessels and Piping Division Conference, Prague, Czech Republic, 15–20 July 2018; p. PVP2018-85058.
9. Takahashi, Y.; Shigeyama, H.; Siefert, J.; Parker, J. A summary of 10 years research on Grade 91 and Grade 92 steel. In *Joint EPRI-123HiMAT International Conference on Advances in High-Temperature Materials*; Shingledecker, J., Takeyama, M., Eds.; ASM International: Materials Park, OH, USA, 2019; pp. 370–378.
10. Siefert, J.A. The Influence of the Parent Metal Condition on the Cross-Weld Creep Performance in Grade 91 Steel. Ph.D. Thesis, Loughborough University, Loughborough, UK, July 2019.
11. Sawada, K.; Sekido, K.; Kimura, K.; Arisue, K.; Honda, M.; Komai, N.; Fukuzawa, N.; Ueno, T.; Shimohata, N.; Nakatomi, H.; et al. Effect of Initial Microstructure on Creep Strength of ASME Grade T91 Steel. *ISIJ Int.* **2020**, *60*, 382–391. [CrossRef]
12. Maruyama, K.; Dewees, D.; Abe, F.; Yoshimi, K. Examinations of equations for creep rupture life with a large creep database on Grade 91 steel. *Int. J. Press. Vessel. Pip.* **2022**, *199*, 104738. [CrossRef]
13. ASME. *ASME Boiler and Pressure Vessel Code-Code Cases: Boilers and Pressure Vessels*; ASME: New York, NY, USA, 2017.
14. ASME. *ASME Boiler and Pressure Vessel Code Section III–Rules for Construction of Nuclear Facility Components-Division 5-High Temperature Reactors*; ASME: New York, NY, USA, 2023.
15. British Energy. *Assessment Procedure R5, Issue 3. Assessment Procedure for the High Temperature Response of Structures*; British Energy: London, UK, 2003.

16. Takahashi, Y. Study on creep-fatigue evaluation procedures for high-chromium steels—Part I: Test results and life prediction based on measured stress relaxation. *Int. J. Press. Vessel. Pip.* **2008**, *85*, 406–422. [CrossRef]
17. Wen, J.F.; Tu, S.T.; Xuan, F.Z.; Zhang, X.W.; Gao, X.L. Effects of Stress Level and Stress State on Creep Ductility: Evaluation of Different Models. *J. Mater. Sci. Technol.* **2016**, *32*, 695–704. [CrossRef]
18. Skelton, R.P. Energy criterion for high temperature low cycle fatigue failure. *Mater. Sci. Technol.* **1991**, *7*, 427–440. [CrossRef]
19. Takahashi, Y.; Dogan, B.; Gandy, D. Systematic evaluation of creep–fatigue life prediction methods for various alloys. *J. Press. Vessel. Technol.* **2013**, *135*, 061204. [CrossRef]
20. Payten, W.M.; Dean, D.W.; Snowden, K.U. A strain energy density method for the prediction of creep–fatigue damage in high temperature components. *Mater. Sci. Eng. A* **2010**, *527*, 1920–1925. [CrossRef]
21. Skelton, R.P. The energy density exhaustion method for assessing the creep–fatigue lives of specimens and components. *Mater. High Temp.* **2013**, *30*, 183–201. [CrossRef]
22. Wang, R.Z.; Zhang, X.C.; Tu, S.T.; Zhu, S.P.; Zhang, C.C. A modified strain energy density exhaustion model for creep–fatigue life prediction. *Int. J. Fatigue* **2016**, *90*, 12–22. [CrossRef]
23. Wang, R.Z.; Zhu, X.M.; Zhang, X.C.; Tu, S.T.; Gong, J.G.; Zhang, C.C. A generalized strain energy density exhaustion model allowing for compressive hold effect. *Int. J. Fatigue* **2017**, *104*, 61–71. [CrossRef]
24. Wang, R.Z.; Zhang, X.C.; Gu, H.H.; Li, K.S.; Wen, J.F.; Miura, H.; Suzuki, K.; Tu, S.T. Oxidation-involved life prediction and damage assessment under generalized creep-fatigue loading conditions based on engineering damage mechanics. *J. Mater. Res. Technol.* **2023**, *23*, 114–130. [CrossRef]
25. Li, K.S.; Wang, J.; Fan, Z.C.; Cheng, L.Y.; Yao, S.L.; Wang, R.Z.; Zhang, X.C.; Tu, S.T. A life prediction method and damage assessment for creep-fatigue combined with high-low cyclic loading. *Int. J. Fatigue* **2022**, *161*, 106923. [CrossRef]
26. Song, K.W.D.; Zhao, L.; Xu, L.; Han, Y. An improved life prediction strategy at elevated temperature based on pure creep and fatigue data: Classical strain controlled and hybrid stress–strain controlled creep-fatigue test. *Eng. Fract. Mech.* **2023**, *289*, 109412. [CrossRef]
27. Zhang, T.; Wang, X.; Xia, X.; Jiang, Y.; Zhang, X.; Zhao, L.; Roy, A.; Gong, J.; Tu, S. A robust life prediction model for a range of materials under creep-fatigue interaction loading conditions. *Int. J. Fatigue* **2023**, *176*, 107904. [CrossRef]
28. Takahashi, Y.; Parker, J.; Gandy, D. Creep-fatigue interaction in Grade 92 steel and its predictability. In *Advances in Materials Technology for Fossil Power Plants: Proceedings from the Seventh International Conference, Waikoloa, HI, USA, 22–25 October 2013*; Gandy, D., Shingledecker, J., Eds.; ASM International: Materials Park, OH, USA, 2014; pp. 667–678.
29. Payten, W.M.; Dean, D.; Snowden, K.U. Analysis of creep ductility in a ferritic martensitic steel using a hybrid strain energy technique. *Mater. Des.* **2012**, *33*, 491–495. [CrossRef]
30. EPRI. *Review of Fabrication and In-Service Performance of a Grade 91 Header*; EPRI: Palo Alto, CA, USA, 2013; p. 3002001831.
31. Nitsche, A.; Mayr, P.; Allen, D. Damage Assessment of Creep Affected Weldments of a Grade 91 Header Component after Long-term High Temperature Service. *Weld. World* **2015**, *59*, 675–682. [CrossRef]
32. ASME. *ASME Boiler and Pressure Vessel Code Section II–Materials-Part A-Ferrous Materials Specifications*; ASME: New York, NY, USA, 2019.
33. Kimura, K.; Yaguchi, M. Re-Evaluation of Long-Term Creep Strength of Base Metal of ASME Grade 91 Type Steel. In Proceedings of the ASME 2016 Pressure Vessels and Piping Conference, British Columbia, VA, Canada, 17–21 July 2016; p. PVP2016-63355.
34. NIMS. *NIMS Creep Data Sheet No. 43A*; NIMS: Tsukuba, Japan, 2014.
35. Spindler, M.W. The prediction of creep damage in type 347 weld metal. Part I: The determination of material properties from creep and tensile tests. *Int. J. Press. Vessel. Pip.* **2005**, *82*, 175–184. [CrossRef]
36. Takahashi, Y. Modelling of rupture ductility of metallic materials over wide ranges of temperatures and loading conditions, part II: Comparison with strain energy-based approach. *Mater. High Temp.* **2020**, *37*, 340–350. [CrossRef]
37. Takahashi, Y. Modelling of rupture ductility of metallic materials over wide ranges of temperatures and loading conditions, part I: Development of basic model. *Mater. High Temp.* **2020**, *37*, 357–369. [CrossRef]